BBA - Molecular Cell Research 1871 (2024) 119575

Contents lists available at ScienceDirect

BBA - Molecular Cell Research

journal homepage: www.elsevier.com/locate/bbamcr

Research paper

Raman microscopy reveals how cell inflammation activates glucose and lipid metabolism

Aleksandra Borek-Dorosz [a], Anna Pieczara [b,c], Jagoda Orleanska [a,c], Krzysztof Brzozowski [a], William Tipping [d], Duncan Graham [d], Ewelina Bik [b,e], Adam Kubrak [a], Malgorzata Baranska [a,b], Katarzyna Majzner [a,*]

[a] Jagiellonian University in Kraków, Faculty of Chemistry, Department of Chemical Physics, 2 Gronostajowa Str., Krakow, Poland
[b] Jagiellonian University in Kraków, Jagiellonian Centre for Experimental Therapeutics (JCET), 14 Bobrzynskiego Str., Krakow, Poland
[c] Jagiellonian University in Kraków, Doctoral School of Exact and Natural Sciences, 11 Lojasiewicza St., Krakow, Poland
[d] Centre for Molecular Nanometrology, WestCHEM, Department of Pure and Applied Chemistry, Technology and Innovation Centre, University of Strathclyde, Glasgow G1 1RD, United Kingdom
[e] Academic Centre for Materials and Nanotechnology, AGH University of Science and Technology, 30 Mickiewicza Str., Krakow, Poland

ARTICLE INFO

Keywords:
High glucose
Cellular metabolism
Inflammation
Endothelial cells
Raman spectroscopy
Coherent spectroscopy

ABSTRACT

Metabolism of endothelial cells (ECs) depends on the availability of the energy substrates. Since the endothelium is the first line of defence against inflammation in the cardiovascular system and its dysfunction can lead to the development of cardiovascular diseases, it is important to understand how glucose metabolism changes during inflammation. In this work, glucose uptake was studied in human microvascular endothelial cells (HMEC-1) in high glucose (HG), and additionally in an inflammatory state, using Raman imaging. HG state was induced by incubation of ECs with a deuterated glucose analogue, while the EC inflammation was caused by TNF-α pre-treatment. Spontaneous and stimulated Raman scattering spectroscopy provided comprehensive information on biochemical changes, including lipids and the extent of unsaturation induced by excess glucose in ECs., induced by excess glucose in ECs. In this work, we indicated spectroscopic markers of metabolic changes in ECs as a strong increase in the ratio of the intensity of lipids / (proteins + lipids) bands and an increase in the level of lipid unsaturation and mitochondrial changes. Inflamed ECs treated with HG, revealed enhanced glucose uptake, and intensified lipid production i.a. of unsaturated lipids. Additionally, increased cytochrome *c* signal in the mitochondrial region indicated higher mitochondrial activity and biogenesis. Raman spectroscopy is a powerful method for determining the metabolic markers of ED which will better inform understanding of disease onset, development, and treatment.

1. Introduction

Endothelial cells (ECs) are the single layer of cells that line the blood and lymphatic vessels, performing a vital role in many cellular functions. It is well known that the endothelium plays an important role among others in nutrient and oxygen exchanges between the bloodstream and surrounding tissues, transport of molecules such as glucose and amino acids, regulating vascular tone, embodying a wide range of homeostatic functions, and regulating blood flow [1–3]. Endothelial metabolism depends on the availability of the energy substrates, but the correlation between inflammation and metabolic reprogramming remains unclear.

The energy-producing process involves four major metabolic pathways: oxidative phosphorylation, glutamine metabolism, fatty acid

Abbreviations: AOM, acoustic-optic modulator; ATP, adenosine triphosphate; Ctrl, control cells; ECs, endothelial cells; ED, endothelial dysfunction; ER, endoplasmic reticulum; Gal, medium containing galactose, glucose-free; Glu, standard medium containing glucose; HG, high glucose; d_7-HG, deuterated glucose (d_7-glucose) in high content; HMEC-1, human dermal microvascular endothelial cells; KMCA, *k*-means cluster analysis; LDs, lipid droplets; RM, Raman microscopy; Rp, Raman probe; OPO, optical parametric oscillator; PCA, Principal Component Analysis; PLSR, Partial Least Square Regression; ROS, reactive oxygen species; RS, Raman spectroscopy; SRL, stimulated Raman loss; SRS, stimulated Raman scattering microscopy; TNF + d_7-HG, cells pre-treated with TNF-α and then incubated with d_7-HG; TNF-α, tumour necrosis factor-alpha.

* Corresponding author.
E-mail address: katarzyna.b.majzner@uj.edu.pl (K. Majzner).

https://doi.org/10.1016/j.bbamcr.2023.119575
Received 31 March 2023; Received in revised form 11 August 2023; Accepted 30 August 2023
Available online 9 September 2023

oxidation, and glycolysis [4]. Glycolysis is a metabolic pathway that converts glucose into pyruvate, and in the next step, to ATP (adenosine triphosphate). ECs exhibit a relatively low content of mitochondria (6–18 %), making glycolysis the preferred source of energy [5], i.e. >85 % of ATP molecules are produced under normal conditions [6,7]. Through glycolysis, ECs reduce the production of reactive oxygen species (ROS), and thus the risk of oxidative stress development [8]. Amino acids, lipids, proteins, and nucleotides are all formed during glycolysis as metabolites of this process [9]. The energy-independent transport of glucose is mediated by members of the facilitative glucose transporter (GLUT) family of glucose carriers that are present on the surface of all cells. Galactose, like glucose, is a monosaccharide that can be used by cells as fuel [10] and is actively transported to cells through the same transporter as glucose [11]. Both monosaccharides are transferred by the uridine diphosphate (UDP) coenzyme in the form of uridine diphosphate-glucose (UDPG) and UDP-galactose (UDPGal). The uptake of dietary glucose and galactose occurs by a secondary active transport process mediated by SGLT1. ECs rely on glucose metabolism, and when it is at some point disturbed or stopped, the cells can switch metabolism and change their energy source from glucose to galactose, if it is present in the medium. The transporter isoforms SGLT-1 (Na+/glucose cotransporter-1) and GLUT1 have been shown to transport D-galactose as efficiently as D-glucose [12,13]. The main pathway for galactose metabolism is considered to be the conversion of galactose to glucose by galactose-1-phosphate (Gal-1-P), UDP-galactose, and glucose-1-phosphate (glucose-1-P) [10,11,14].

Endothelial dysfunction (ED) refers to a variety of functional changes that are linked to metabolic alterations. Altered glucose metabolism is reflected by specific plasma amino acids and lipids [15]. High levels of glucose (HG) in the bloodstream can deteriorate the antioxidant defence mechanism and cause mitochondrial oxidative stress, while overproduction of ROS can further lead to endoplasmic reticulum (ER) stress and apoptosis [16]. ER stress refers to a chronic perturbation that affects ER homeostasis and is primarily characterized by the accumulation of misfolded proteins, which disrupts the balance of the protein folding capacity of the ER to keep up with cellular demand [17–19]. Oxidative stress and ER stress caused by the HG level in the bloodstream lead to ED, and hence to the development of diabetes [16,17]. The onset of diabetes itself further raises glucose levels, which continues to cause changes in the mitochondria and the ER. Detailed analysis of cell metabolism leads to a better understanding of these processes.

Raman microscopy (RM) is a method widely used in cell analysis. RM measurement is characterized by high spectral resolution, and full chemical information about the studied sample [20–22]. The analysis is based on the identification of characteristic spectral patterns that can be used also for quantification. Measurements can be carried out simultaneously for all components of fixed or live cells in their physiological environment [23,24]. RM should be considered as a method of choice for cellular lipids analysis since these components exhibit a high cross-section for Raman scattering.

In recent years, the use of labels in RM enhanced the specificity in targeting components of complex biological samples. Labelling, widely used in fluorescence-based biological assays, was also successfully applied in RM on cell activity studies [25,26]. Labelled molecular imaging can track lipids uptake and their metabolism [27], or changes in mitochondrial activity [28]. Labels in RM are called Raman probes (Rp) that usually contain a moiety that targets certain organelles, e.g. mitochondria [29], nuclei [30], lipids [31], or ER [32]. Another characteristic part of Rp is a molecular structure providing the unique Raman signal that is detected in the silent spectral region (1800–2700 cm^{-1}) of biological samples. Hence, most often Rp contains alkyne, nitrile, or isotopically substituted groups [30,33].

The characteristic spectroscopic signature of Rp and the advantages of stimulated Raman scattering (SRS) microscopy provide a new possibility for Raman-based cellular studies. SRS belongs to the group of nonlinear spectroscopic techniques, which have been developed to improve real-time vibrational imaging by overcoming the low signal level associated with spontaneous Raman imaging [34]. By combining SRS with various Rp, cells can be measured in a specific and sensitive way with insight into their metabolism and function [35–37], and track drugs [38].

It has been shown that glucose metabolism can be studied using SRM (Spontaneous Raman Microscopy) and Rp [39–41]. It is an alternative to fluorescent dyes, which can cause abnormal cell activity and undesired interactions due to the large size of fluorochromes [33]. Labelled SRS is a promising strategy to track glucose metabolism. By specific molecular substitution in a glucose molecule (isotopes or an alkyne tag), it is possible to detect it in the silent region of the Raman spectrum [42].

Glucose-based Rp has been used to study the uptake and monitoring of glucose metabolism in cells and tissues [36,40,42]. Application of 3-O-propargyl-D-glucose (3-OPG) allowed distinguishing cancer cells with distinct metabolic activity and revealed heterogeneous glucose uptake patterns in tumour tissues and neuronal culture [36]. Deuterium-labelled glucose enabled de novo tracking of the synthesis of macromolecules in biological samples and macromolecule type-specific metabolic mapping with high spatial resolution [25,35,39–41].

Although this is an important area of research, little is still known about ECs physiopathology and the impact of HG on ECs – too many factors are involved [16]. In this work, we studied the cellular changes in lipid content and composition related to glucose metabolism when cells were cultured in glucose-containing and glucose-free media, in two groups of cells, i.e., normal, and inflamed cells. The HG state was induced by EC incubation with d_7-glucose (d_7-HG), while cell inflammation was stimulated by using TNF-α. RM and SRM measurements provided comprehensive and reliable information about the biochemical composition of ECs. Detailed analysis of subcellular glucose metabolism provided a better evaluation of lipid alterations in the inflamed endothelium.

2. Materials and methods

2.1. Sample preparation

Human microvascular endothelial cells (HMEC-1) were cultured in standard medium MCDB131 (Gibco Life Technologies, 5 mM glucose), supplemented with 2 % hydrocortisone, 10 mM L-glutamine, 10 % fetal bovine serum (FBS) and antibiotics (100× solution with penicillin, streptomycin, and amphotericin B). Cells were seeded directly on calcium fluoride slides (CaF_2, 25 mm 2 mm, Pike Technologies, USA), which were placed in 6-well plates and incubated in a humidified cell culture incubator. After the appropriate time (24 h) required to achieve approximately 70% confluence, the medium was changed, and cells were incubated with a d_7-glucose-enriched medium (d_7-HG).

Three variants of cell culture and incubation with HG were tested. In the first variant, HMEC-1 cells were cultured in MCDB131 medium (Glu) supplemented with 30 mM d_7-HG (Sigma Aldrich). The incubation time with d_7-HG was 24, 48, and 72 h. In variant no. 2, cells were also incubated with 30 mM d_7-HG for 24, 48, and 72 h, but cells were cultured in glucose-free MCDB131 medium, in which glucose is replaced by galactose (Gal, without L-glutamine, without glucose, and no Phenol Red, Gendepot). This variant was then modified, and in the culture protocol during incubation with d_7-HG incubation, the medium was changed every 24 h (variant no. 3). In this variant, cells were incubated with a fresh batch of glucose and a fresh portion of nutrients to maintain the possibility of continuous and constant uptake of d_7-HG.

The second part of the work on d_7-HG-induced changes in cellular metabolism was dedicated to the comparison of endothelial response in healthy (Ctrl) and inflamed cells. Cells were cultured with glucose-free medium (Gal) replaced every 24 h. To induce the inflammation, HMEC-1 cells were pre-incubated with TNF-α (concentration 10 ng/ml) for 24 h according to the previously described protocols [27,43–45] and then with d_7-HG (30 mM) for 24, 48, and 72 h. After incubation, cells

were fixed with 2.5 % glutaraldehyde (5 min) at room temperature and gently washed three times with PBS (Gibco). Subsequently, the fixed cells were kept in PBS and stored at a constant temperature of 4 °C until RM and SRS measurements were performed. Cells were measured directly up to a few days after fixation.

2.2. Fluorescent and immunofluorescent staining

HMEC-1 cells were seeded in 96-well plates and allowed to attach overnight. After TNF-α pre-treatment (concentration 10 ng/ml) for 24 h and then with d_7-HG (30 mM) for 24, 48, and 72 h cells were fixed with 4 % buffered formalin for 10 min. Protein levels of VCAM-1 and ICAM-1 were assessed using immunofluorescent staining. Primary antibodies were added for 24 h after the initial permeabilization and blocking step. Cells were washed twice in PBS prior to the addition of secondary antibody, Cy3 goat-anti-mouse, Biotin-SP-conjugated goat-anti-rat and Alexa Fluor 594 streptavidin. The following primary antibodies were used: mouse ICAM-1 (ThermoFisher) and rat VCAM-1 (ThermoFisher). Additionally, cells were stained with Hoechst 33342 (Invitrogen; 1:1000) to counterstain nuclei and, thus, evaluate the cytotoxicity. All fluorescent images were captured with CQ1 Yokogawa, an automated fluorescence microscope, with using a 20× objective. Fluorescence intensity was calculated by using spot intensity algorithm.

2.3. Raman imaging

Raman measurements were made using a confocal Raman imaging system (WITec alpha 300, WITec GmbH, Ulm, Germany) and a 63× water dipping objective (Zeiss W Plan-Apochromat

63×, NA = 1, Oberkochen, Germany). Fixed cells were measured in PBS solution at room temperature. In all experiments, the laser excitation of 532 nm was used. Raman imaging was performed with a step size of 0.5 μm. The integration time was 0.5 s per spectrum. To improve the signal-to-noise ratio of d_7-HG-treated cells in a normal and inflamed state, cells were imaged with a 40× water dipping objective (Zeiss, W Plan-Apochromat VISIR, NA = 1, Oberkochen, Germany), the step size was 1 μm, and the integration time was 0.5 s per spectrum with a full laser power of 30 mW (measured before the objective). For each sample, only morphologically undamaged cells were measured, with no visible signs of abnormalities, with at least 15 cells per group.

Raman spectra of standard d_7-glucose (Sigma Aldrich, solid-state) were obtained with the application of the 20× air objective (Nikon CFI S Plan Fluor ELWD, NA = 0.45, Melville, U.S.A) after placing a microgram quantity of the standard sample on the CaF_2 slide. The spectrum was measured with a maximum laser power (30 mW) by collecting and averaging 10 accumulations with an integration time equal to 0.5 s.

2.4. SRS measurement and data analysis

SRS imaging was performed using the homemade setup located at the Faculty of Chemistry, Jagiellonian University in Krakow. We used a 2-ps laser (Fluence Lazurite, Warsaw, Poland) with

20 MHz repetition rate based on a fiber laser producing 1029-nm Stokes beam with 450 mW of average power with a built-in optical parametric oscillator (OPO) that produces tunable wavelength beam in the range of 750–950 nm with an average power of 100 mW. In our setup, the Stokes beam is modulated with an acousto-optic modulator (AOM) with 4 MHz and the stimulated Raman loss (SRL) signal in the pump beam is collected. The signal is retrieved with the use of Stanford Research Systems SR865A lock-in amplifier, sent to the electronics, and stored by the software provided by WITec. A 40× air objective (Olympus, UPLXAPO40X NA = 0.95, Oberkochen, Germany) was used to focus the laser beams on the sample. The transmitted pump beam was collected by a 50× water-dipping objective lens (Nikon, MRD07620 NA = 1 Melville, U.S.A).

2.5. Post-processing of spectral data

Spectral data pre-processing and analysis were performed in WITec Project FIVE 5.1 Plus software. The pre-processing included cosmic ray removal and baseline correction (shape mode, shape size 100). In the next steps, *k*-means cluster analysis (KMCA) was performed for each single-cell Raman image. KMCA enabled to group of the spectra into classes based on their similarities. For each cell, the spectra were classified into 3 groups: background, nuclear area (colour-coded in blue), and cytoplasm (colour-coded in grey). Spectra grouped as a cytoplasm class were next subclustered into the perinuclear area (colour-coded in brown), LDs (colour-coded in orange), and the CD class if possible (colour-coded in pink). Spectra grouped to each class were then averaged and extracted for further analysis.

Distinct Raman distribution images of HMEC-1 cells were obtained by integration of the selected maker bands: organic matter (2830–3030 cm^{-1}), lipids (2830–2900 cm^{-1}), nuclear area (775–795 cm^{-1}), cytochrome *c* (750–760 cm^{-1}) and additionally the structures with C—D bond (glucose and glucose metabolites) (2190–2250 cm^{-1}).

2.6. Raman image analysis

Morphology analysis was performed on the KMCA images. The areas of the entire cell class and the lipid class were calculated for each cell using the Image Statistics function in WITec Project FIVE 5.1 Plus software. In a further step, the ratio of lipid area/cell area was calculated and to verify the statistical significance of changes in cell morphology, a one-way analysis was performed (ANOVA model with a Tukey post-hoc test) using the OriginPro 2020 software (Origin Lab Corporation, Northampton, USA). Results are presented in bars that indicate the mean value (the end of the box) and the SD (standard deviation, whiskers). Statistically significant differences are marked with stars (*$p<0.05$, **$p<0.01$, ***$p<0.001$).

Ratiometric Raman images were generated using WITec software and following the approach described by Jamieson et al. [46]. First, a 2D image of the protein distribution was generated by integration over the 2900–2960 cm^{-1} spectral range, based on which the mask of the cellular area was defined and extracted to eliminate from the hyperspectral matrix of Raman image noncellular pixels of the background. The matrix with mask image was then multiplied by the Raman distribution images obtained for the lipids (by integration of the marker band over the 2830–2900 cm^{-1} spectral range) and proteins (integration for the 2930 cm^{-1} marker band over the 2900–2960 cm^{-1} spectral range). Elimination of the noncellular pixels from the Raman image was necessary to avoid possible artefacts from the ratio analysis conducted on the noise signal of the baseline. The value of the ratio (2850 cm^{-1} / (2850 cm^{-1} + 2930 cm^{-1})) for each colour-coded Raman image of a cell was calculated using a calculator tool. The values of 2850 cm^{-1} / (2930 cm^{-1} + 2850 cm^{-1}) ratio were next visualised in box plots using OriginPro 2020 software.

SRS images were processed with WITec Project PLUS 5.1 software and extracted. All SRS images were equally subjected to background subtraction and duplicated. In the same way, the SRS images were processed to obtain the area occupied by the cells. The intensity of the areas occupied by lipid components was measured with the "Analyse Particle" function, a built-in function in ImageJ software (the National Institutes of Health and the Laboratory for Optical and Computational Instrumentation (LOCI, University of Wisconsin)). The threshold was manually specified in ImageJ and kept at a similar level for each image analyzed, and then the intensity of the areas occupied by lipid components was measured. SRS images were analyzed using WITec Project PLUS 5.1 software.

2.7. Chemometric analysis

Chemometric analysis was performed on the average spectra

obtained for each cell from the lipid or cytoplasm classes using the PLS-Toolbox Solo Mia software from Eigenvector Research Inc. (Mason, USA). The first step of the analysis was pre-processing, which included smoothing (third-order polynomial and 15 points), baseline correction, and normalization with the multiplicative signal correction option (MSC mean). The final set of spectra was subject to the Mean Center and Clutter options [47] also in the PLS-Toolbox Solo Mia software. Principal component analysis (PCA) was performed in the 600–2450 cm^{-1} spectral range. The final presentation of scores and loadings was prepared using OriginPro 2020 software.

Partial least squares (PLS) regression, which is a supervised chemometric method, was also applied to construct a discriminant model that could visualise time-dependent changes (24 d_7-HG, 48 d_7-HG, 72 d_7-HG with or without pre-treatment with TNF-α). To build the PLS model, all available spectroscopic data were used to calibrate and validate the model. The PLS model was constructed based on the 600–2450 cm^{-1} spectral range with the following pre-processing of Raman spectra: constant offset elimination, multiplicative scattering correction, internal standard, and vector normalization. PLS was performed using OPUS 7.0 software (Bruker Optik GmbH, USA).

3. Results and discussion

3.1. Glucose uptake by EC depends on incubation time with HG and culture medium type

The uptake of d_7-HG by HMEC-1 was studied by RM based on analysis of C—D vibration occurring in the silent spectral region (2190–2250 cm^{-1}). HMEC-1 were incubated in a standard medium containing normal 5 mM glucose (Glu) and glucose-free medium (Gal), respectively, and supplemented with d_7-HG (30 mM). HMEC-1 were cultured on Gal medium for 48 and 72 h, respectively, and the impact of medium replacement every 24 h (Gal everyday) was investigated. Representative Raman images of cells incubated with d_7-HG for 48 h (48 d_7-HG) on various media, i.e. variants no. 1 (Glu), 2 (Gal), and 3 (Gal everyday), with corresponding KMCA images, are presented in Fig. 1A. Raman images were constructed by the integration of selected bands to visualise major cellular compartments, i.e. organic matter (2800–3030 cm^{-1}, C—H stretching), LDs (2830–2900 cm^{-1}, symmetric ν(C—H)), nucleus (775–795 cm^{-1}, cytosine in DNA/RNA) and subcellular areas with an enriched accumulation of d_7-HG –CD (2190–2250 cm^{-1}, C—D stretching). In Fig. 1B the spectra of five clusters identified for cells incubated for 48 h with d_7-HG (Gal everyday) are presented. A comparison of the spectrum taken from HMEC-1 with the one of the d_7-glucose standard in the solid state (black line) confirms the identification of the C—D band. The C—D stretching modes were observed at 2124, 2174, and 2243 cm^{-1} [40,42].

The spectra of cells cultured in Glu medium, even after incubation with d_7-HG for 72 h, showed no C—D signal and thus no d_7-HG uptake. However, when the cells were cultured in Gal medium and supplemented with d_7-HG for 48 and 72 h, we found that only about 5 % of all measured cells exhibited clusters with the characteristic C—D band. The KMCA image clearly shows the presence of d_7-HG within the cytoplasmic region (Fig. 1). These cells were excluded from further analysis (PCA, PLS-DA) to avoid a strong impact of d_7-HG Raman features on the overall classification. In most spectra taken from cells, the C—D band was not observed, but the uptake of d_7-glucose can be identified by an increased baseline in the 2100–2450 cm^{-1} range (Fig. 2A). Similar situation was when the medium was replaced every 24 h. Approx. 5–10 % of the measured cells exhibited a C—D Raman signal within the cytoplasm (Fig. 1A), but an increased baseline in the 2100–2450 cm^{-1} range was observed in all measured cells. The C—D band in Raman spectra collected from cells on Glu medium and treated with d_7-HG was relatively intense when ECs were grown for both 48 and 72 h (Fig. 2).

The uptake of d_7-HG was slightly greater with increasing incubation time, which can be observed as an increase in the silent region, especially for a lipidic class. In the literature, a similar pattern in the silent region was also observed, with only a slight increase in the baseline in the range around 1900–2250 cm^{-1}, so our observations are in agreement with the previously reported work in HeLa cells and other tumour

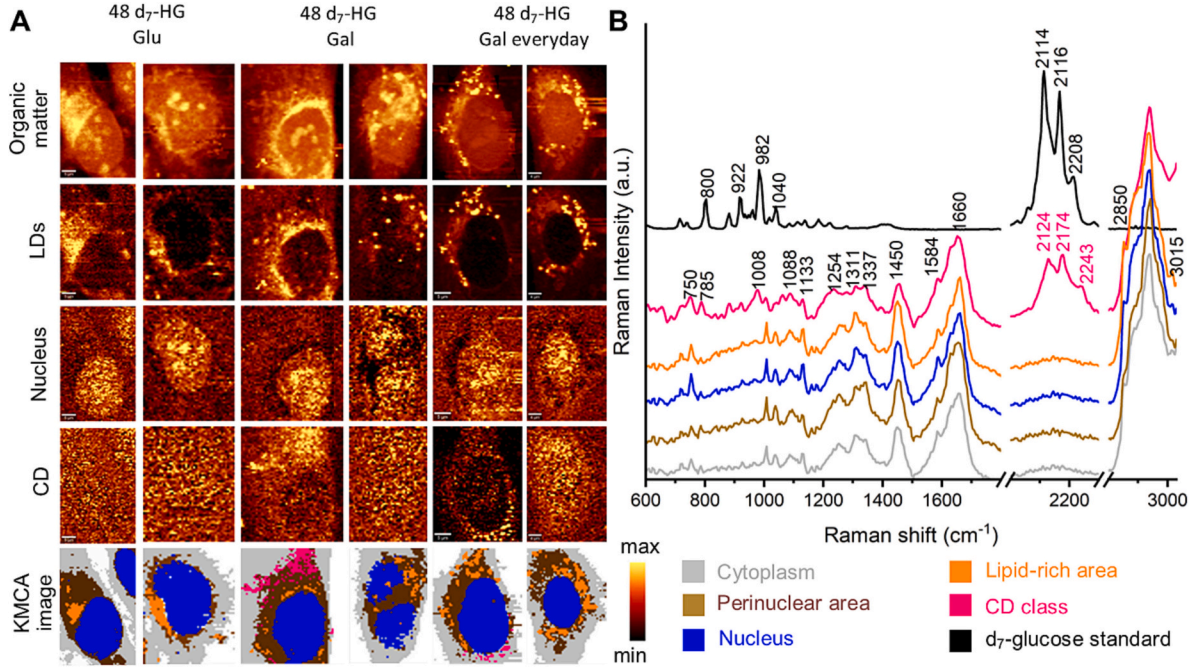

Fig. 1. Raman images of HMEC-1 cultured in glucose-containing and glucose-free media supplemented with d_7-HG incubated for 48 h with 30 mM d_7-HG (A): organic matter (cellular area, 2800–3030 cm^{-1}), lipids (LD, 2830–2900 cm^{-1}), nucleus (775–795 cm^{-1}) and C—D band area (CD, 2190–2450 cm^{-1}). KMCA spectra from 24 d_7-HG Glu everyday together with Raman spectrum of the d_7-glucose standard (black) (B). The Raman spectra presented in the fingerprint region (600–1800 cm^{-1}) and the silent region (2100–2250 cm^{-1}) were multiplied by factor 1.5 for clearer data visualization. The assignment of KMCA classes is as follows: nucleus - blue, cytoplasm – grey, lipid reach area – orange, perinuclear area – brown, CD class - magenta.

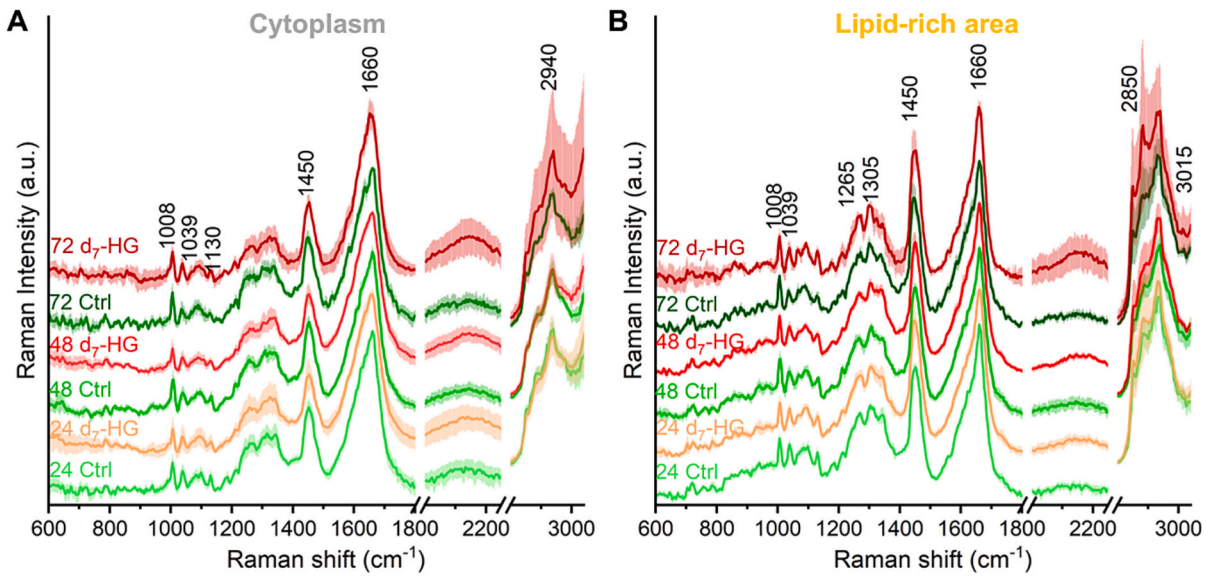

Fig. 2. Effect of the incubation time with d_7-HG on the biochemical profile of the cytoplasm and lipids in HMEC-1. Average Raman spectra (±SD) of the cytoplasm (A) and lipid-rich (B) areas of HMEC-1 incubated with d_7-HG in Glu medium. Raman spectra in the fingerprint region (600–1800 cm^{-1}) and the silent region (2100–2250 cm^{-1}) were multiplied by 1.5 for clearer visualization.

cells [35,39]. What is more, the spectral profile of d_7-HG-treated cells changes with time in C—H stretching region (2800–3030 cm^{-1}) (Fig. 2), especially the intensity of the bands at 2850 and 1305 cm^{-1} collected in the lipid-rich area of the cells. It may suggest that the changes caused by the d_7-glucose uptake are related to lipid metabolism.

3.2. Glucose in the culture medium affects endothelial metabolism

In Fig. 3 the averaged spectra of cytoplasm and lipid class, which were extracted during KMCA from control after treatment with d_7-HG are shown. Fig. 3A (Glu and Gal media supplemented with d_7-HG) shows results obtained from cells cultured for 24, 48, and 72 h, and indicate changes in endothelial metabolism. By changing the medium from Glu to Gal, the metabolism of HMEC-1 changes to the metabolism of fatty acids, which is manifested by spectral markers of lipids. In Fig. 3A a comparison of the average spectra of the lipid-rich area of cells incubated with d_7-HG for 24–72 h in Glu and Gal media is presented.

For cells cultured in Gal, the band at 1440 cm^{-1} (scissoring mode in CH_2/CH_3; $\delta(CH_2/CH_3)$) is more intense when compared to the spectrum of cells cultured in Glu media. Similar changes were seen for spectra from the perinuclear area classes (data not shown). To quantitatively compare the changes in lipid composition, the unsaturation level was calculated for single-cell averaged spectra extracted from the lipid-rich class (Fig. 3B). The integral intensity ratio of the bands at 1660 cm^{-1} [ν(C=C)], and 1440 cm^{-1} [CH_2], served to estimate whether the level of lipids changed when cells were cultured in Glu and Gal media over time, with and without the supplementation of d_7-HG [48]. The ANOVA indicated that ECs cultured in glucose-free conditions exhibited different biochemical profiles of lipids and a lower level of unsaturation for cells incubated with d_7-HG for 48 and 72 h.

An increase in the intensity of the band at 1440 cm^{-1} in the spectra of HMEC-1 cultured in Gal medium was observed together with a higher intensity of the signal at 1305 cm^{-1} (twisting of the CH_2/CH_3 groups in lipids) and 2850 cm^{-1}. Therefore, it can be concluded that the presence or absence of a normal glucose level (5 mM) affects endothelium metabolism. Galactose, like glucose, is a monosaccharide that can be used by cells as fuel [10] and is actively transported to cells through the same transporter as glucose [11]. Galactose treatment has been previously noted to enhance cell lipid content [49], therefore, our results confirmed that with limited availability of glucose, HMEC-1 cells switched to galactose metabolism. The main pathway for galactose metabolism is considered to be the conversion of galactose to glucose by galactose-1-phosphate (Gal-1-P), UDP-galactose, and glucose-1-phosphate (glucose-1-P) [10,11,14].

3.3. Inflammation of the cells changes their glucose uptake and cellular lipid composition

To model inflammation, HMEC-1 were pre-treated with TNF- α for 24 h and then incubated with d_7-HG (30 mM) for 24, 48, and 72 h (Gal everyday). Cell viability was assessed based on number of cells estimated by Hoechst staining. TNF- α and d_7-HG did not cause decrease the viability of HMEC-1 cell line (Fig. S1) in time dependent manner when compared to the control group. The occurrence of endothelial inflammation after TNF- α treatment was evaluated by an overexpression (Fig. S1) of intercellular adhesive (ICAM-1) and vascular cell adhesion (VCAM-1) molecules. After 24 h of TNF-α pre-incubation, inflammatory response was confirmed, whereas after incubation with d7-HG. Immunofluorescence staining revealed that 24 h of incubation of control and inflamed HMEC-1 cells with d_7-HG (d_7-HG and TNF+ d_7-HG) also results in ICAM-1 and VCAM-1 overexpression. Increased overexpression of ICAM-1 and VCAM-1 was observed over time only for set of cells incubated with d_7-HG, but this result is rather the effect of increased proliferation (based on nuclear counterstaining) than the inflammation process.

Then the spectral profile of healthy and inflamed cells was compared. As reported previously, HMEC-1 in the inflammation state exhibited an increased number of LDs, mainly composed of unsaturated lipids [43,50]. The results in Fig. 4 are in agreement with previously reported data [40,41,43,50,51]. Representative Raman images obtained by integration of the marker bands of selected compartments, i.e., organic matter (2800–3030 cm^{-1}), lipids (2830–2900 cm^{-1}), cytochrome *c* (775–795 cm^{-1}), together with KMCA images are presented in Fig. 4.

To capture the differences in the lipid content, the ratiometric analysis of the bands at 2850 cm^{-1} and 2930 cm^{-1}, assigned respectively to lipids and proteins, was also performed. Calculated for each point of the single-cell Raman image, the value of the integral intensity ratio (2850 cm^{-1} / (2850 cm^{-1} + 2930 cm^{-1}) [46,52] confirmed that TNF-α treated cells exhibit higher lipid content compared to control. The

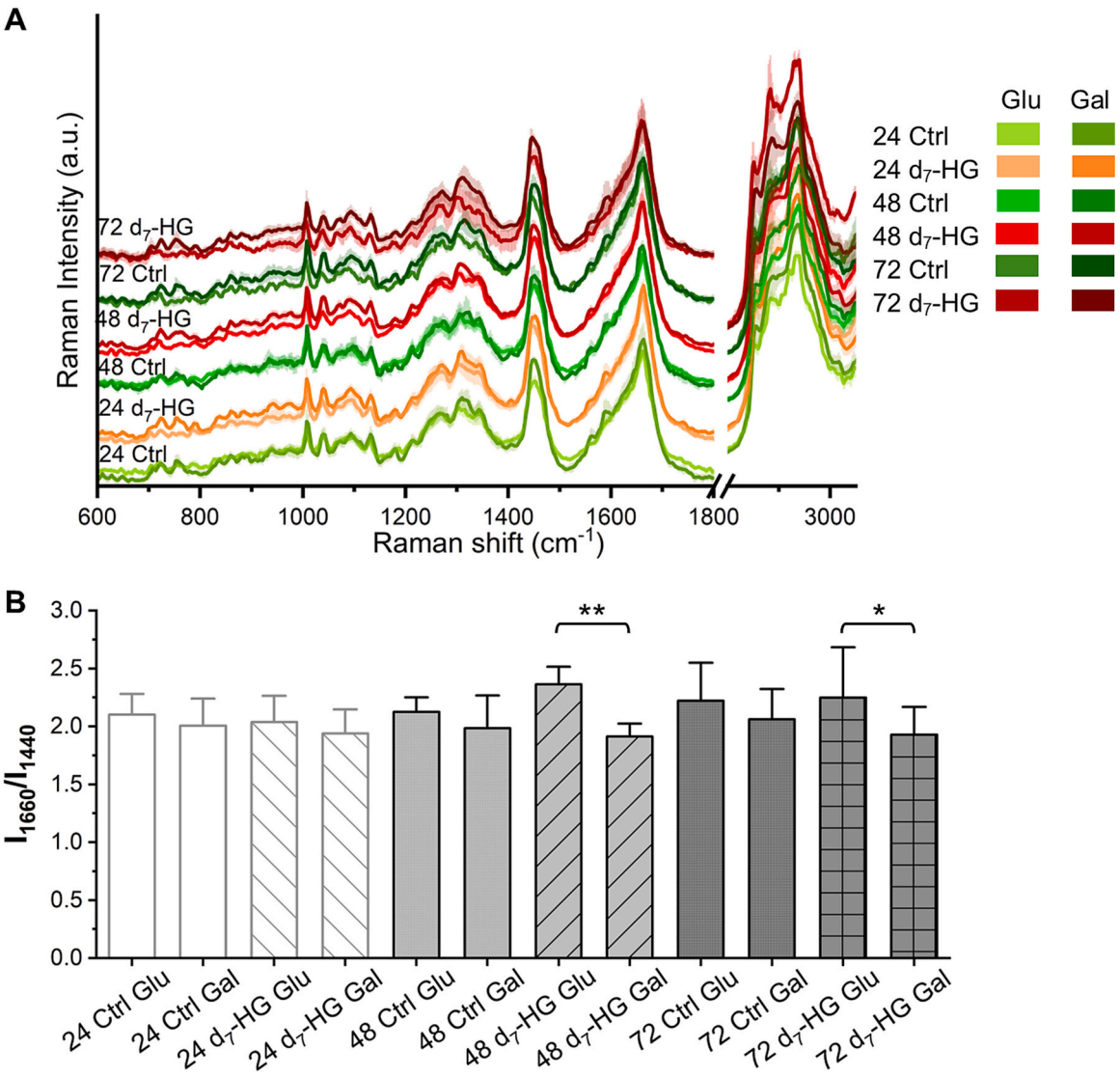

Fig. 3. Effect of the type of culture medium on the lipid profile in HMEC-1. Comparison of mean spectra (±SD) for the lipid-rich class of cells incubated with d_7-HG in Glu and Gal media for a different time frame (A). The Raman spectra presented in the fingerprint (600–1800 cm^{-1}) were multiplied by a factor of 1.5 for clearer visualization. Analysis of the unsaturation level of lipids from the lipid-rich class calculated as integral intensities ratio of bands at 1660 and 1440 cm^{-1}. Values are given as mean ± SD, *$p < 0.05$, **$p < 0.01$.

most prominent changes were observed for cells cultured for 48 and 72 h, however, based on visual inspection of the images of lipid distribution, no clear impact of inflammation on lipid metabolism was found. However, analysis of the Raman images obtained through a ratiometric approach (I_{2850}/ (I_{2850}+I_{2930})) showed some differences in the subcellular morphology of d_7-HG-treated cells. To quantify those differences, a morphological analysis was performed (Fig. 5A). The obtained results revealed that d_7-HG uptake increased lipid production and inflammation, which also contributes to these processes. Changes in lipid metabolism manifest themselves in Raman images in two ways, i.e., by increasing the intensity of marker bands of lipids and by a larger subcellular area occupied by lipids (area of lipids/area of cells). The ratio of the area of lipids divided by the total area of the cell body was calculated based on KMCA images (orange class/whole-cell class; Fig. 4). The results of the ratiometric analysis (the ratio of integral intensities: I_{2850} / (I_{2850} + I_{2930}) allowed a semiquantitative evaluation of the total content of lipids in the perinuclear area. The results of the ratio I_{2850} / (I_{2850}+I_{2930}) were next analyzed with one-way ANOVA to verify if the observed changes are statistically significant (Fig. 5B).

The analysis confirmed the increase in the production of lipids due to d_7-HG treatment, especially in the case of cells incubated for 48 and 72 h (Fig. 5B). TNF-α treatment increased lipid production in ECs as described previously, and it is known that this proinflammatory factor leads to eicosanoid release, which is fundamental to the inflammatory process [27,43,50,53]. The results in Fig. 5 show that not only inflammation changes the content of lipids in the ECs but also the uptake of d_7-HG influences the metabolism of cells and the production of lipids. Taking into account the metabolic pathway, d_7-HG can be transformed into lipids, nucleic acids, and proteins [40]. The presented results clearly show that longer exposure to d_7-HG resulted in increased lipid production. This mechanism is enhanced when ECs are inflamed.

To check whether the TNF-α pre-treatment impacts the chemical composition of lipids in ECs upon d_7-HG treatment, the analysis of the unsaturation level of lipids was conducted. The ratio of the integral intensities of the bands at 1660 and 1440 cm^{-1} calculated for the spectra of the lipid-rich class of EC revealed statistically significant changes in unsaturation (Fig. 6A). This observation clearly indicates qualitative changes in the lipid profile. The results described above for analysis of unsaturation of lipids of ECs cultured in Glu and Gal medium showed that glucose-free medium affected metabolism and changed the lipid

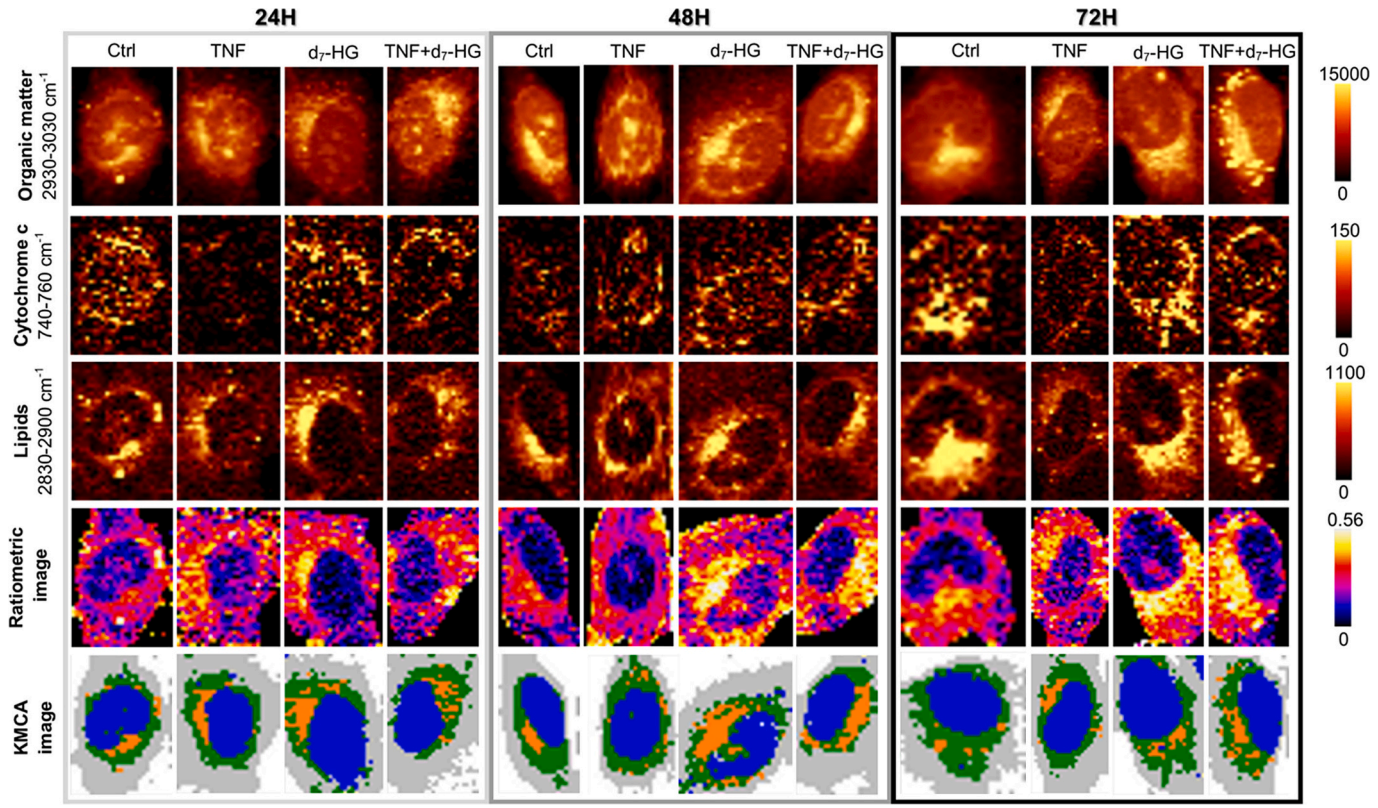

Fig. 4. Raman images of HMEC-1 in Gal medium supplemented with d_7-HG for 24, 48 and 72 h in normal and inflammation conditions. Representative Raman chemical images obtained by the integration over 2830–3030 cm^{-1} (organic matter), 2830–2900 cm^{-1} (lipids), 740–760 cm^{-1} (cytochrome *c*). Corresponding false-colour KMCA images displaying the distribution of selected cell components (nucleus (blue), perinuclear area (green), LDs (lipid-rich area), cytochrome *c* (green)). Colour-coded results from ratiometric Raman analysis ((I_{2850} / (I_{2850} + I_{2930})) representing the distribution of lipids.

composition. The lipid spectra of cells cultured in the Gal medium exhibited a lower unsaturation level when compared to the standard medium (Fig. 3). The results in Fig. 6A (Gal) allowed several conclusions to be drawn.

The uptake of d_7-HG changes the unsaturation of lipids of normal and TNF-α pre-treated cells cultured for 48 and 72 h of incubation (d_7-HG and TNF+ d_7-HG) in comparison to the Control. Observed changes related to the increased unsaturation enhanced when ECs were pre-treated with TNF-α (d_7-HG vs TNF+ d_7-HG). However, the Ctrl groups did not reveal any differences in the level of lipids with time. On the other hand, TNF-α pre-treated HMEC-1 cells showed changes in the lipid profile with time. After 24 h from TNF-α pre-treatment, the cells manifested an increased unsaturation level of lipids, which confirmed the induced inflammatory mechanism with the involvement of eicosanoids, and after 72 h of culture, the unsaturation level was lowered close to the initial value.

Analysis of the band assigned to the C—D stretching mode, which is an indicator of d_7-HG uptake, showed that inflammation does not affect d_7-HG uptake in a short incubation time, but in the case of the cells incubated for 48 and 72 h, a slight decrease in the intensity of C—D band can be seen, which can suggest a decrease in the uptake under inflammatory conditions [27,54]. However, when only sets of cells treated with d_7-HG were considered, the results again confirmed that a longer incubation time favours d_7-HG uptake.

3.4. Inflammation of the cells changes their glucose metabolism

Cellular metabolism is difficult to track, especially glucose metabolism, which depends on many factors. As shown above, the Raman signatures related to metabolic changes are very subtle and not distinctive in the spectra. To identify Raman signatures of d_7-HG-induced changes in cellular metabolism and to investigate whether other alterations occur than those described above, both PCA (Fig. 7A–F) and PLS (Fig. 7G & H) were applied. The chemometric approach was performed in two spectral windows: 600–2450 and the sum of 600–2450 and 2830–3030 cm^{-1} (data not shown).

Several variants for PCA have been tested. In the first approach, the analysis was performed on single-cell average spectra of lipid-rich class from all tested sets of cells (Fig. 7A & B, 24–72 h: Ctrl, TNF, d_7-HG, TNF+ d_7-HG). Then, to capture changes caused by d_7-HG uptake and TNF-α pre-treatment, the PCA was performed only on single-cell average spectra of the lipid-rich class collected from each investigated time point. The unsupervised approach, employing PCA, resulted in a clear separation of the spectra along PC-1 into 2 groups: Ctrl and TNF-α pre-treated cells with TNF-α (PC-1(−)) vs. treated (PC-1(+)). The PC-1 loading plot was characteristic of the spectra of cells treated with d_7-HG (Fig. 7B) and indicated Raman features in the range of the C—D stretching mode (2124 and 2184 cm^{-1}) together with features at 1337, 1290, and 1029 cm^{-1}. Analysis of the spectral profile suggested a higher contribution of proteins in the lipid-rich area of d_7-HG-treated cells. The Raman bands at 1029 cm^{-1} can be assigned to the hydroxyproline content and the C—C stretching of proteins, while 1290 and 1337 cm^{-1} to the amide III bands in proteins. The Raman characteristic originating from the C—D stretching mode (2124 and 2184 cm^{-1}) also suggests a higher contribution from the CH_3 stretching, which is characteristic of proteins. The C—D stretching mode in the CH_2 group would be expected at ca. 2108–2110 cm^{-1} [27].

A similar signature was observed in the PCA presented in Fig. 7C & D where the separation of spectra collected from cells cultured for 72 h was observed along PC-1. However, in this approach, the spectra of TNF-pre-treated cells separated from the spectra of healthy ECs along PC-2 (Fig. 7C) (Ctrl and TNF groups) based on hemoproteins signals. PCA of

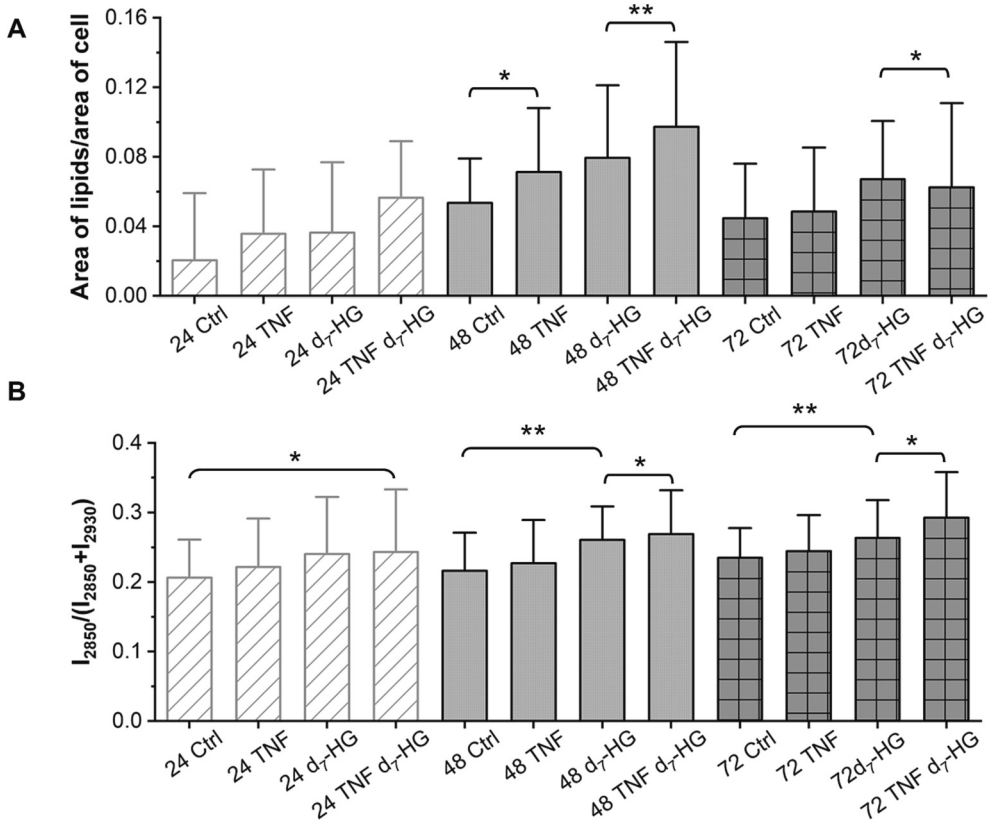

Fig. 5. Ratiometric analysis of the distribution and content of lipids in healthy and inflamed HMEC-1 cultured in Gal medium supplemented with d_7-HG treatment. Analysis of subcellular area occupied by lipids obtained based on KMCA results. Quantitative analysis of the ratio of lipid area/area of the cell (A) and the integral intensities ratio of I_{2850} / (I_{2850} + I_{2930}) for Raman images (B). Values are given as mean ± SD, *p < 0.05, **p < 0.01.

spectra collected only from cells incubated with d_7-HG (d_7-HG, TNF+ d_7-HG) revealed the progression of changes over time (Fig. 7E & F). The scores plot in Fig. 7E clearly shows that most distinct changes occur when comparing spectra from cells exposed to d_7-HG for 24 and 72 h, while part of the spectra from the 48 h experiment exhibits some similarities with PC-1(+) and partly with PC-1(−). For 72 h of incubation of HMEC-1 in Gal medium with d_7-HG on Raman spectra, the most discriminant features are indicated as those corresponding to C—D vibrations (2139, 2187 cm^{-1}), unsaturated lipids (1660 cm^{-1}) and hemoproteins (750 cm^{-1}).

PLS models were calibrated and validated (one leave-out cross-validation) in a set of spectra from cells cultured in Gal medium for 24, 48, and 72 h with d_7-HG (Fig. 7 G, red) and additionally, TNF-α pretreated (TNF+ d_7-HG, Fig. 7G, magenta). Both models exhibit time dependence, and analysis of regression coefficients allows one to identify similar Raman features indicated as latent variables for regression. Moreover, the regression coefficients are similar to the Raman signature presented on PC-1 loadings.

Analysis of the spectral silent region allows the identification of 2 or 3 maxima at the C—D stretching marker band (Fig. 7B, D, F, H). Different positions in the loadings of the C—D stretching mode are related to the isotopic effect due to changes In the reduced mass of the C—D bond and vibrational force constant, k. Zhang et al. [40] used SRS measurements and a spectral unmixing approach to show that the maximum of the C—D band can be used to assign the contribution of lipids (CD_L 2190 cm^{-1}), proteins (CD_P 2150 cm^{-1}) and DNA (CD_D 2125 cm^{-1}). Based on the spontaneous Raman measurement and chemometric analysis, it is very challenging to establish whether such an assignment can be applied. Based on previously reported results, the contribution of lipids should be observed around 2110 cm^{-1} [27]. In summary, C—D bands are clearly visible in the spectra of lipids occurring in normal and inflamed cells incubated with d_7-HG and their intensity increases with time. Furthermore, changes in the lipid metabolism of cells due to d_7-HG incubation were enhanced in inflamed cells.

A similar analysis was also conducted on the single-cell average spectra from the cytoplasm class (colour-coded in grey in Fig. 4, Fig. S2). This approach was taken to verify whether biochemical changes due to d_7-HG treatment occurred outside of the perinuclear area dominated by lipids and mitochondria. The results obtained from PCA (Fig. S2A–F) and PLS (Fig. 2G & H) revealed a similar spectroscopic signature to that obtained for the lipid-rich class. For the cytoplasm, the largest differences in biochemical profile due to d_7-HG uptake and inflammation were found in proteins, hemoproteins, and lipids, especially in unsaturation. Score plots (Fig. S2A) indicate clear discrimination of cells cultured with d_7-HG supplemented or not with Gal medium. The main spectroscopic difference was found again for variables associated with the C—D stretching mode (2124 and 2184 cm^{-1}), and proteins (1331, 1280, and 1023 cm^{-1}).

Furthermore, an analysis of the time dependence on metabolic changes was performed (Fig. S2E & F). As previously, we have found that the most distinct spectra belong to the groups of cells after 24 and 72 h d_7-HG treatment, while the spectra of cells cultured for 48 h are located in between. At 72 h, characteristic bands correspond to the C—D vibrations (2184 cm^{-1}), lipids (1660 cm^{-1}) and hemoproteins (755 cm^{-1}), while cells exposed to d_7-HG only for 24 h exhibit the most prominent Raman features at 815, 1204, 1572 and 1602 cm^{-1}.

To verify whether observed changes in lipid profile can be detected by analysis of single cell average spectra the PCA analysis was conducted on an independent set of cells that served as a test group. Single cell average spectra of at least 35 cells per group were subjected to PCA and obtained results revealed Raman features that are related with changes in lipids content (Figs. S3 & S4). The obtained results indicate that

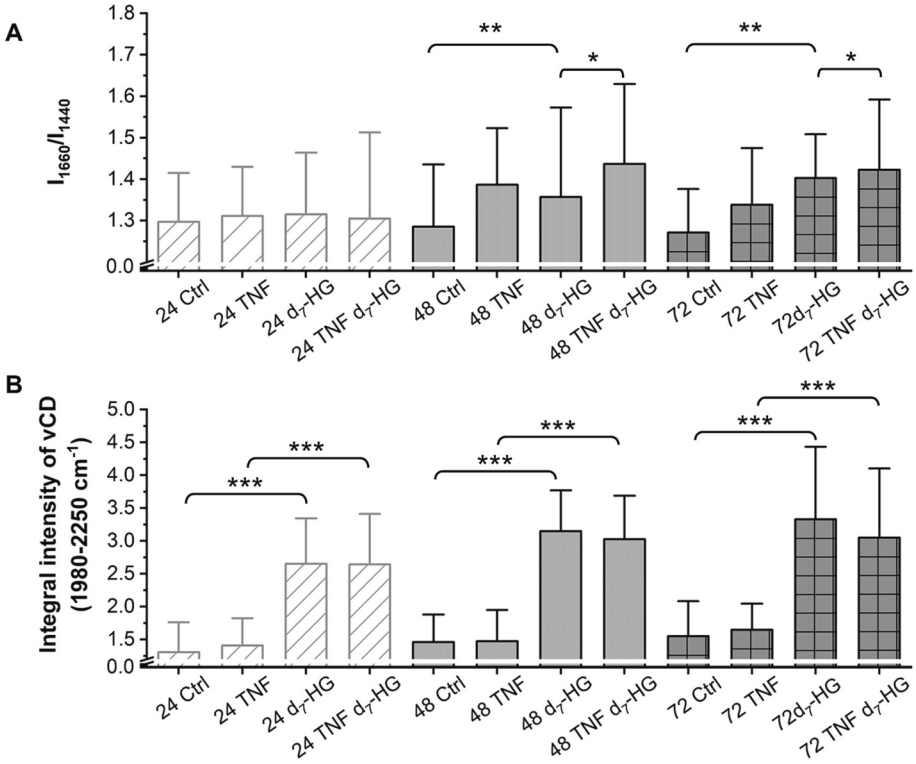

Fig. 6. Impact of inflammation on lipid composition in HMEC-1 cultured in glucose-free medium and incubated with d_7-HG. Quantitate analysis of the level of unsaturation calculated based on the integral intensity ratio of the bands at 1660 and 1440 cm^{-1} for average single-cell spectra of lipid class (A) and the integral intensity of the Raman bands assigned to CD_2/CD_3 stretching mode (ν_{CD}) in the spectral range of 1980–2250 cm^{-1}. Values are given as mean ± SD, *$p < 0.05$, **$p < 0.01$, ***p<0,001.

contribution from those changes to spectroscopic fingerprint of cells is significant.

The changes associated with inflammation on glucose uptake and metabolism were also studied employing SRS microscopy. SRS images provided information about the subcellular localization of LDs as a result of inflammation (Fig. 8). SRS imaging enabled the visualization of lipid and protein content (2930 cm^{-1}) and lipid distributions (2850 cm^{-1}), however, due to a very low signal from deuterated glucose, SRS image acquisition for C—D band was difficult. To model inflammation, HMEC-1 was pre-treated with TNF- α for 24 h and then incubated with d_7-HG (30 mM) for 24, 48, and 72 h (Gal everyday). Then the spectral profiles of Ctrl and inflamed cells were compared.

Analysis of the SRS images showed that TNF-treated cells have a higher lipid content than Ctrl. As reported previously, HMEC-1 in the inflammation state exhibit an increased number of LDs [43,50]. So, the results in Fig. 8 are in agreement with previously reported data. The most noticeable modifications were identified in cells that had been cultured for 24 and 72 h. The results of the relative SRS intensity were analyzed with one-way ANOVA to verify if the observed changes are statistically significant (Fig. 8). SRS results are in agreement with the presented above results from spontaneous Raman imaging when compared to data from healthy and inflamed glucose-treated cells. Ratiometric results presented in Fig. 5B for analysis of changes in lipid contribution of d_7-HG-treated cells have shown a statistically significant increase in lipid content for TNF-α pre-treated cells at the $p < 0.05$. SRS imaging confirmed the above results, and due to the time of single-cell imaging, the analysis of the much larger group of cells has shown that glucose uptake and metabolism in inflamed cells differ significantly from that presented by healthy cells ($p < 0.001$). RM and SRS are both Raman-based spectroscopic techniques, but they differ in the observed phenomenon, measurement time and sensitivity. When it comes to spectroscopic imaging of cellular lipid fractions quickly and reliably, SRS imaging is undoubtedly the most efficient method and at the same time provides detailed insight into the morphology of cells. Although Raman imaging provides a comprehensive biochemical analysis, its measurement capacity is significantly lower. Both employed spectroscopic techniques that allowed the acquisition of spectral information from cells, but with increased speed of measurement when SRS microscopy was applied, hence a higher number of cells was measured in a short time. Furthermore, the application of chemometric analysis techniques to SRS microscopy of cellular lipids has been reported to visualise the underlying biochemical processes at the single-cell level [52–55]. Our results show that RM advantage is a screening for the identification of markers of molecular changes while SRS can serve as a method for fast and reliable identification of its presence. Fast high-resolution imaging enables not only to quantify observed molecular and metabolic changes but also to evaluate morphological alterations induced by studied factors. Therefore, by combining RM and SRS we provide detailed insight into the subcellular changes at three levels: molecular, metabolic, and morphological.

4. Conclusions

In this work, a comprehensive spectroscopic analysis of the biochemical phenotype of the endothelium that exhibits adaptive cellular metabolism is described. The biochemical alteration observed for HMEC-1 cultured in glucose-containing and glucose-free media enabled the capture of

a switch in cellular metabolism. These changes were even more pronounced after prior inflammatory stimulation of the cells, implying that inflammatory mediators modulate glucose uptake and its metabolism. In the inflammation state, an increase in HG uptake was observed over time, correlated with an increase in the content of lipids and a higher level of their unsaturation.

Obtained results revealed that HMEC-1 with limited access to glucose switched their metabolism to fatty acids. We have also found

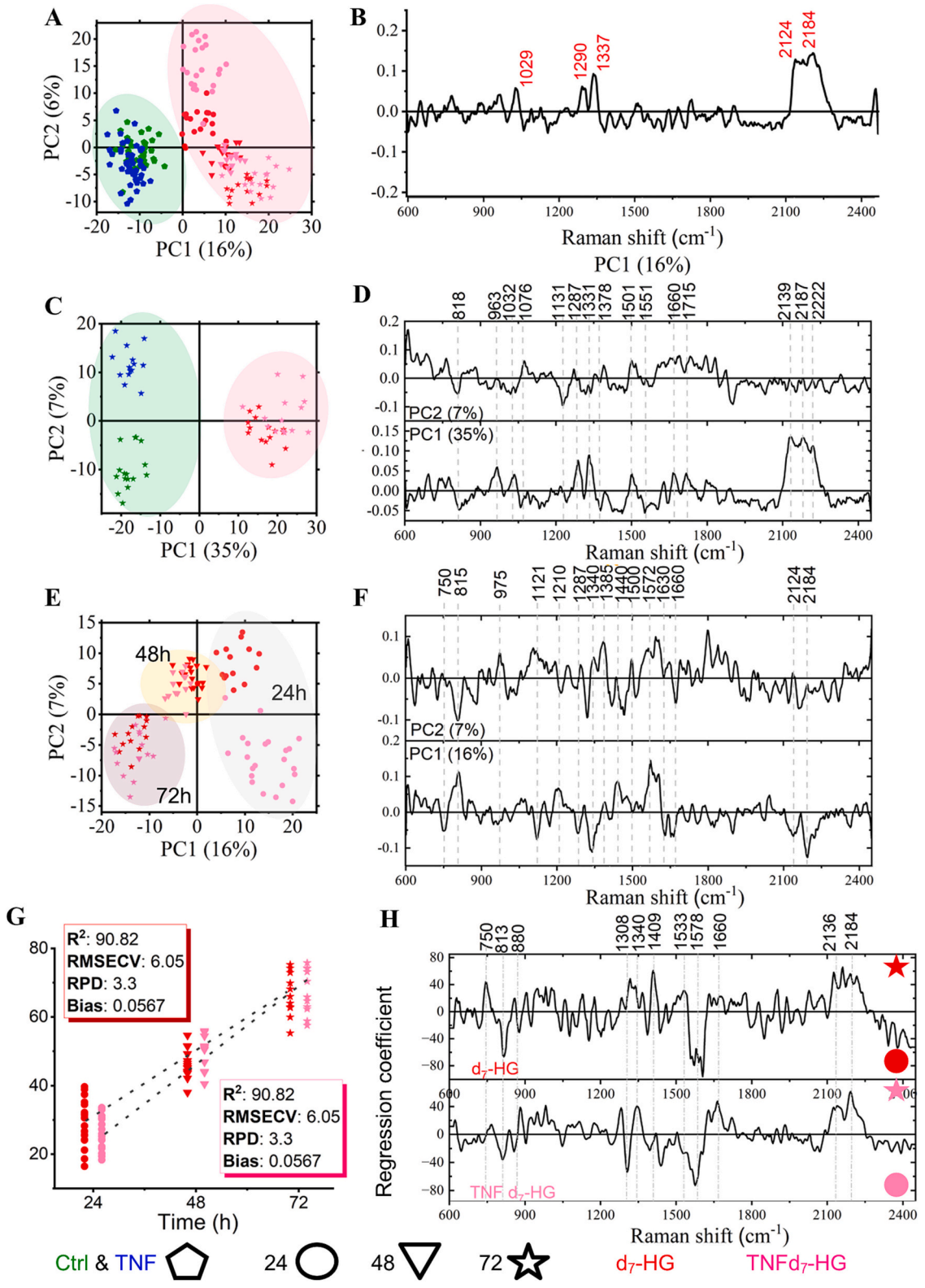

Fig. 7. Chemometric analysis of lipid-rich spectra of healthy and inflamed cells incubated with d_7-HG. PCA of Control, TNF-α pre-treated, and cells incubated with d_7-HG (d_7-HG and TNF+ d_7-HG) from all time points investigated (24–72 h) (A, B). PCA of Ctrl, TNF-α pre-treated, and cells incubated with d_7-HG (d_7-HG and TNF+ d_7-HG) for 72 h (C, D). PCA of a set of spectra from cells incubated with d_7-HG (d_7-HG and TNF+ d_7-HG) from all investigated time points (24–72 h) (E, F). PLS models (G, H) trained and validated for the spectra of healthy cells (red) and TNF-α pre-treated cells (magenta) cultured in Gal medium supplemented with d_7-HG for 24 h (dot), 48 h (triangle), and 72 h (star).

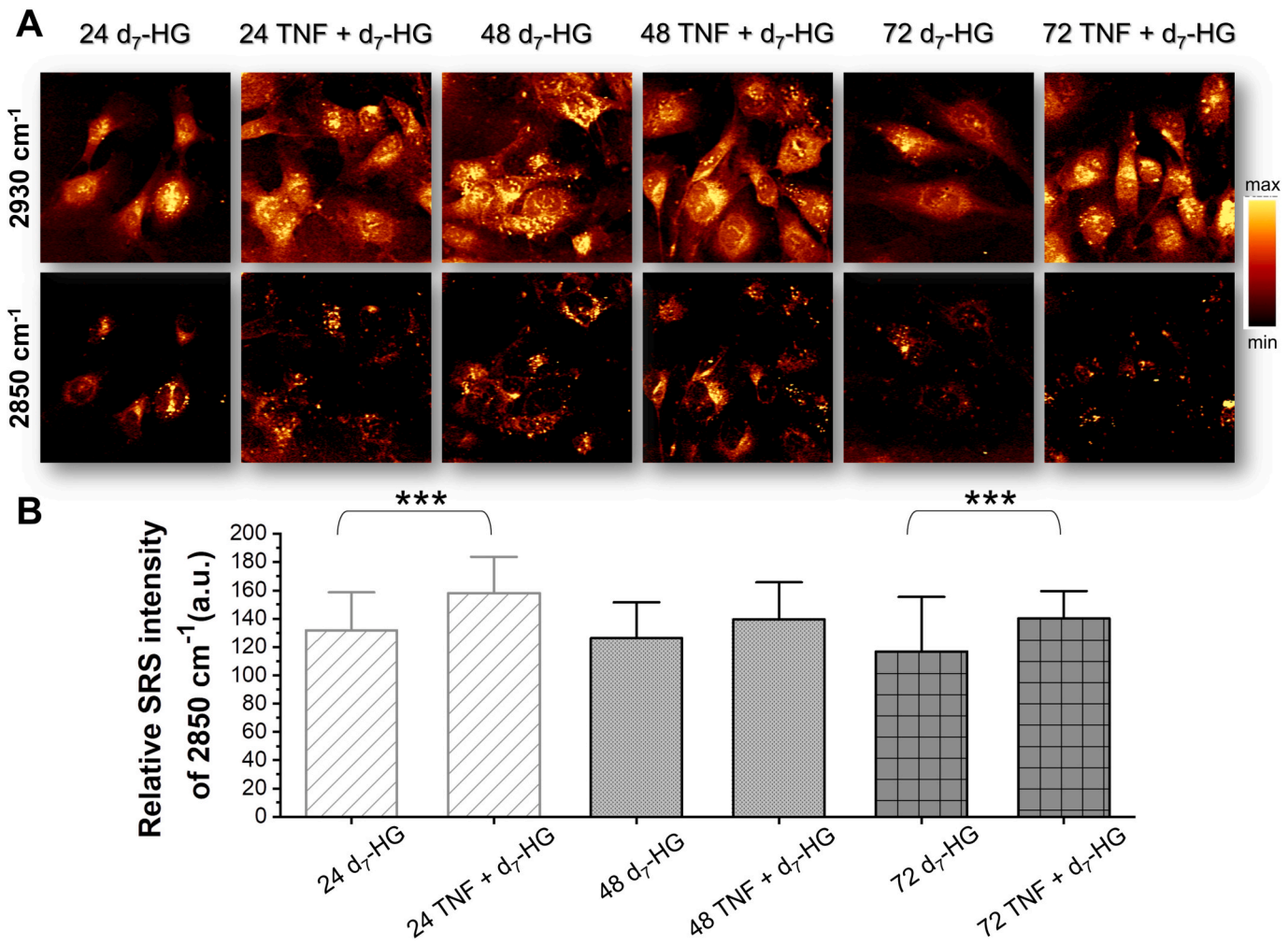

Fig. 8. Impact of inflammation on lipid composition in HMEC-1 cultured in glucose-free medium (Gal) and incubated with d_7-HG. Relative SRS intensity of lipids (2850 cm^{-1}) in d_7- glucose treated cells. Values are given as mean ± SD, ***p<0,001.

that ECs treated with d_7-HG in inflammation change their metabolism to be more active, which was reflected in increased glucose uptake and increased lipid production. In addition, mitochondrial markers suggest increased metabolic activity and mitochondrial biogenesis.

CRediT authorship contribution statement

ABD: Measurements, Data analysis, Investigation, Visualization, Writing - original draft. **AP:** Measurements, Data analysis, Investigation, Writing - original draft. **JO:** Data analysis. **KB:** Measurements, Data analysis, Review, and Editing. **WT:** Data curation, Writing – review. **DG:** Writing – review. **EB:** Data analysis. **AK:** Data analysis. **MB:** Conceptualization, Validation, Supervision, Writing, Review and Editing. **KM:** Supervisions, Conceptualisation, Investigation, Writing, Review, and Editing. All authors read and approved the final manuscript.

Declaration of competing interest

The authors declare that they have no competing financial interests.

Data availability

Data will be made available on request.

Acknowledgements

The study was supported by a grant from the National Science Centre Poland (NCN) (OPUS15 no. UMO-2018/29/B/ST4/00335 to MB). The authors are grateful to MSc Renata Budzynska (JCET UJ) for cell culturing and help with sample preparation. EB is supported by the Foundation for Polish Science (FNP).

Appendix A. Supplementary data

Supplementary data to this article can be found online at https://doi.org/10.1016/j.bbamcr.2023.119575.

References

[1] H.F. Galley, N.R. Webster, Physiology of the endothelium, Br. J. Anaesth. 93 (2004) 105–113.
[2] W.C. Aird, Phenotypic heterogeneity of the endothelium: I structure, function, and mechanisms, Circ. Res. 100 (2007) 158–173.
[3] P. Rajendran, T. Rengarajan, J. Thangavel, Y. Nishigaki, D. Sakthisekaran, G. Sethi, I. Nishigaki, The vascular endothelium and human diseases, Int. J. Biol. Sci. 9 (2013) 1057–1069.
[4] M. Potente, P. Carmeliet, The link between angiogenesis and endothelial metabolism, Annu. Rev. Physiol. 79 (2017) 43–66.
[5] G. Eelen, P. de Zeeuw, L. Treps, U. Harjes, B.W. Wong, P. Carmeliet, Endothelial cell metabolism, Physiol. Rev. 98 (2018) 3–58.
[6] S.W.S. Leung, Y. Shi, The glycolytic process in endothelial cells and its implications, Acta Pharmacol. Sin. 432 (43) (2021) 251–259.

[7] W. Du, L. Ren, M.H. Hamblin, Y. Fan, Endothelial cell glucose metabolism and angiogenesis, Biomedicines 9 (2021) 1–17.
[8] B. Yetkin-Arik, I.M.C. Vogels, P. Nowak-Sliwinska, A. Weiss, R.H. Houtkooper, C.J. F. Van Noorden, I. Klaassen, R.O. Schlingemann, The role of glycolysis and mitochondrial respiration in the formation and functioning of endothelial tip cells during angiogenesis, Sci. Rep. 9 (2019) 1–14.
[9] J. Zhu, C.B. Thompson, Metabolic regulation of cell growth and proliferation, Nat. Rev. Mol. Cell Biol. 20 (2019) 436–450.
[10] R.D. Semba, M. Gonzalez-Freire, R. Moaddel, K. Sun, E. Fabbri, P. Zhang, O. D. Carlson, M. Khadeer, C.W. Chia, N. Salem Jr., L. Ferrucci, Altered plasma amino acids and lipids associated with abnormal glucose metabolism and insulin resistance in older adults, J. Clin. Endocrinol. Metab. 103 (2018) 3331–3339.
[11] E. Burgos-Morón, Z. Abad-Jiménez, A.M. de Marañón, F. Iannantuoni, I. Escribano-López, S. López-Domènech, C. Salom, A. Jover, V. Mora, I. Roldan, E. Solá, M. Rocha, V.M. Víctor, Relationship between oxidative stress, ER stress, and inflammation in type 2 diabetes: the battle continues, J. Clin. Med. 8 (2019) 1385.
[12] M.P. Murphy, Mitochondrial dysfunction indirectly elevates ROS production by the endoplasmic reticulum, Cell Metab. 18 (2013) 145–146.
[13] H.M.A. Zeeshan, G.H. Lee, H.R. Kim, H.J. Chae, Endoplasmic Reticulum Stress and Associated ROS, Int. J. Mol. Sci. 17 (2016) 327.
[14] G. Bánhegyi, P. Baumeister, A. Benedetti, D. Dong, Y. Fu, A.S. Lee, J. Li, C. Mao, E. Margittai, M. Ni, W. Paschen, S. Piccirella, S. Senesi, R. Sitia, M. Wang, W. Yang, Endoplasmic reticulum stress, Ann. N. Y. Acad. Sci. 1113 (2007) 58–71.
[15] E.B. Hanlon, R. Manoharan, T.W. Koo, K.E. Shafer, J.T. Motz, M. Fitzmaurice, J. R. Kramer, I. Itzkan, R.R. Dasari, M.S. Feld, Prospects for in vivo Raman spectroscopy, Phys. Med. Biol. 45 (2000).
[16] D. Coling, B. Kachar, Principles and application of fluorescence microscopy, Curr. Protoc. Mol. Biol. 44 (1998) 1–11.
[17] A.F. Palonpon, M. Sodeoka, K. Fujita, Molecular imaging of live cells by Raman microscopy, Curr. Opin. Chem. Biol. 17 (2013) 708–715.
[18] E. Smith, G. Dent, Modern Raman Spectroscopy, Wiley, 2019.
[19] K. Małek, Vibrational Spectroscopy: From Theory to Applications, Wydawnictwo Naukowe PWN, 2016.
[20] Y. Li, B. Shen, S. Li, Y. Zhao, J. Qu, L. Liu, Review of stimulated Raman scattering microscopy techniques and applications in the biosciences, Adv. Biol. 5 (2021) 1–17.
[21] A. Adamczyk, E. Matuszyk, B. Radwan, S. Rocchetti, S. Chlopicki, M. Baranska, Toward Raman subcellular imaging of endothelial dysfunction, J. Med. Chem. 64 (2021) 4396–4409.
[22] A. Borek-Dorosz, A. Pieczara, Krzysztof Czamara, M. Stojak, E. Matuszyk, Katarzyna Majzner, K. Brzozowski, A. Bresci, D. Polli, Malgorzata Baranska, What is the ability of inflamed endothelium to uptake exogenous saturated fatty acids? A proof-of-concept study using spontaneous Raman, SRS and CARS microscopy, Cell. Mol. Life Sci. 7912 (79) (2022) 1–15.
[23] A. Pieczara, E. Matuszyk, P. Szczesniak, J. Mlynarski, M. Baranska, Changes in the mitochondrial membrane potential in endothelial cells can be detected by Raman microscopy, Spectrochim. Acta - Part A Mol. Biomol. Spectrosc. 286 (2023), 121978.
[24] H. Yamakoshi, A. Palonpon, K. Dodo, J. Ando, S. Kawata, K. Fujita, M. Sodeoka, A sensitive and specific Raman probe based on bisarylbutadiyne for live cell imaging of mitochondria, Bioorg. Med. Chem. Lett. 25 (2015) 664–667.
[25] H. Yamakoshi, K. Dodo, A. Palonpon, J. Ando, K. Fujita, S. Kawata, M. Sodeoka, Alkyne-tag Raman imaging for visualization of mobile small molecules in live cells, J. Am. Chem. Soc. 134 (2012) 20681–20689.
[26] B. Radwan, A. Adamczyk, S. Tott, K. Czamara, K. Kaminska, E. Matuszyk, M. Baranska, Labeled vs label-free raman imaging of lipids in endothelial cells of various origins, Molecules 25 (2020) 5752.
[27] E. Matuszyk, A. Adamczyk, B. Radwan, A. Pieczara, P. Szcześniak, J. Mlynarski, K. Kamińska, M. Baranska, Multiplex Raman imaging of organelles in endothelial cells, Spectrochim. Acta - Part A Mol. Biomol. Spectrosc. 255 (2021), 119658.
[28] Y. Li, Z. Wang, X. Mu, A. Ma, S. Guo, Raman tags: novel optical probes for intracellular sensing and imaging, Biotechnol. Adv. 35 (2017) 168–177.
[29] J.-X. Cheng, W. Min, Y. Ozeki, D. Polli, Stimulated Raman Scattering Microscopy: Techniques and Applications, 1st ed., 2021.
[30] F. Hu, M.R. Lamprecht, L. Wei, B. Morrison, W. Min, Bioorthogonal chemical imaging of metabolic activities in live mammalian hippocampal tissues with stimulated Raman scattering, Sci. Rep. 6 (2016).
[31] F. Hu, Z. Chen, L. Zhang, Y. Shen, L. Wei, W. Min, Vibrational imaging of glucose uptake activity in live cells and tissues by stimulated Raman scattering, Angew. Chem. Int. Ed. 54 (2015) 9821–9825.
[32] L. Wei, F. Hu, Z. Chen, Y. Shen, L. Zhang, W. Min, Live-cell bioorthogonal chemical imaging: stimulated Raman scattering microscopy of vibrational probes, Acc. Chem. Res. 49 (2016) 1494–1502.
[33] W.J. Tipping, M. Lee, A. Serrels, V.G. Brunton, A.N. Hulme, Stimulated Raman scattering microscopy: an emerging tool for drug discovery, Chem. Soc. Rev. 45 (2016) 2075–2089.
[34] F. Hu, L. Shi, W. Min, Biological imaging of chemical bonds by stimulated Raman scattering microscopy, Nat. Methods 16 (2019) 830–842.
[35] L. Zhang, L. Shi, Y. Shen, Y. Miao, M. Wei, N. Qian, Y. Liu, W. Min, Spectral tracing of deuterium for imaging glucose metabolism, Nat. Biomed. Eng. 3 (2019) 402–413.
[36] J. Li, J.-X. Cheng, Direct visualization of de novo lipogenesis in single living cells, Sci. Rep. 4 (2014) 6807.
[37] R. Long, L. Zhang, L. Shi, Y. Shen, F. Hu, C. Zeng, W. Min, Two-color vibrational imaging of glucose metabolism using stimulated Raman scattering, Chem. Commun. 54 (2017) 152–155.
[38] L.E. Jamieson, C. Wetherill, K. Faulds, D. Graham, Ratiometric Raman imaging reveals the new anti-cancer potential of lipid targeting drugs, Chem. Sci. 9 (2018) 6935–6943.
[39] N.B. Gallagher, D. O'Sullivan, M. Palacios, The Effect of Data Centering on PCA Models, (n.d.).
[40] K. Czamara, K. Majzner, M.Z. Pacia, K. Kochan, A. Kaczor, M. Baranska, Raman spectroscopy of lipids: a review, J. Raman Spectrosc. 46 (2015) 4–20.
[41] M. Dashty, A quick look at biochemistry: carbohydrate metabolism, Clin. Biochem. 46 (2013) 1339–1352.
[42] A.I. Coelho, G.T. Berry, M.E. Rubio-Gozalbo, Galactose metabolism and health, Curr. Opin. Clin. Nutr. Metab. Care 18 (2015) 422–427.
[43] E.T. Kase, N. Nikolić, S.S. Bakke, K.K. Bogen, V. Aas, G.H. Thoresen, A.C. Rustan, Remodeling of oxidative energy metabolism by galactose improves glucose handling and metabolic switching in human skeletal muscle cells, PLoS One 8 (2013) 59972.
[44] G. Liu, G.E. Hale, C.L. Hughes, Galactose metabolism and ovarian toxicity, Reprod. Toxicol. 14 (2000) 377–384.
[45] K. Czamara, K. Majzner, A. Selmi, M. Baranska, Y. Ozaki, A. Kaczor, Unsaturated lipid bodies as a hallmark of inflammation studied by Raman 2D and 3D microscopy, Sci. Rep. 7 (2017) 40889.
[46] M.Z. Pacia, M. Sternak, L. Mateuszuk, M. Stojak, A. Kaczor, S. Chlopicki, Heterogeneity of chemical composition of lipid droplets in endothelial inflammation and apoptosis, Biochim. Biophys. Acta, Mol. Cell Res. 1867 (2020), 118681.
[47] M. Mangini, M.A. Ferrara, G. Zito, S. Managò, A. Luini, A.C. De Luca, G. Coppola, Cancer metabolic features allow discrimination of tumor from white blood cells by label-free multimodal optical imaging, Front. Bioeng. Biotechnol. 11 (2023) 1–12.
[48] L.E. Jamieson, A. Li, K. Faulds, D. Graham, Ratiometric analysis using Raman spectroscopy as a powerful predictor of structural properties of fatty acids, R. Soc. Open Sci. 5 (2018), 181483.
[49] E. Bik, J. Orleanska, L. Mateuszuk, M. Baranska, K. Majzner, S. Chlopicki, Raman and fluorescence imaging of phospholipidosis induced by cationic amphiphilic drugs in endothelial cells, Biochim. Biophys. Acta, Mol. Cell Res. 1869 (2022), 119186.
[50] A. Borek-Dorosz, M. Grosicki, J. Dybas, E. Matuszyk, M. Rodewald, T. Meyer-Zedler, M. Schmitt, J. Popp, K. Malek, M. Baranska, Identification of inflammatory markers in eosinophilic cells of the immune system: fluorescence, Raman and CARS imaging can recognize markers but differently, Cell. Mol. Life Sci. 79 (2022).
[51] A. Pieczara, A. Borek-Dorosz, S. Buda, W. Tipping, D. Graham, R. Pawlowski, J. Mlynarski, M. Baranska, Modified glucose as a sensor to track the metabolism of individual living endothelial cells - observation of the 1602 cm−1 band called "Raman spectroscopic signature of life", Biosens. Bioelectron. 230 (2023), 115234.
[52] W.J. Tipping, L.T. Wilson, C. An, A.A. Leventi, A.W. Wark, C. Wetherill, N.C. O. Tomkinson, K. Faulds, D. Graham, Stimulated Raman scattering microscopy with spectral phasor analysis: applications in assessing drug–cell interactions, Chem. Sci. 13 (2022) 3468–3476.
[53] D. Fu, X.S. Xie, Reliable cell segmentation based on spectral phasor analysis of hyperspectral stimulated Raman scattering imaging data, Anal. Chem. 86 (2014) 4115–4119.
[54] P. Wang, B. Liu, D. Zhang, M.Y. Belew, H.A. Tissenbaum, J.-X. Cheng, Imaging lipid metabolism in live *Caenorhabditis elegans* using fingerprint vibrations, Angew. Chem. Int. Ed. 53 (2014) 11787–11792.
[55] E.W. Hislop, W.J. Tipping, K. Faulds, D. Graham, Label-free imaging of lipid droplets in prostate cells using stimulated Raman scattering microscopy and multivariate analysis, Anal. Chem. 94 (2022) 8899–8908.